ROYAL SOCIETY
OF CHEMISTRY

PAPER

Synthesis and evaluation of alkali-activated blast-furnace slag materials with high compressive strength and CO2 capture properties

Tania Ariadna García-Mejía, [a] Efraín Ovando-Shelley [b] and Rosa María Ramírez-Zamora *[a]

This study investigated the synthesis and evaluation of alkali-activated materials (AAMs) derived from industrial by-products, targeting their dual function as sustainable alternatives to Portland cement and as CO_2 adsorbents. AAMs were prepared using iron blast furnace slag and calcined alumina. Response surface methodology was employed to optimize the formulation, focusing on the SiO_2/Na_2O and Si/Al molar ratios and the liquid/solid ratio to enhance mechanical and adsorption performance. The synthesized AAMs were characterized via compressive strength testing, nitrogen physisorption, Fourier transform infrared spectroscopy (FTIR), and scanning electron microscopy (SEM). CO_2 capture performance was assessed using thermogravimetric analysis. The optimal formulation ($SiO_2/Na_2O = 0.5$, Si/Al = 2.0) exhibited a compressive strength of 35.6 MPa after 7 days, a specific surface area of 49.3 m^2 g^{-1}, and a CO_2 adsorption capacity of 0.80 mmol g^{-1} at 35 °C and $P_{CO_2} = 0.2$. SEM analysis revealed a homogeneous porous structure with micropores (1–3 nm) and mesopores. FTIR spectra showed characteristic bands at 1410 and 1470 cm^{-1}, associated with O−C−O stretching, confirming CO_2 adsorption. The findings demonstrate a simple and effective approach for developing multifunctional AAMs with promising mechanical properties and carbon capture capabilities.

1 Introduction

In the past few decades, CO_2 emissions have continued to rise at an alarming rate, contributing significantly to global warming. The efforts to enhance energy efficiency and adopt low-carbon energy sources have progressed; however, the reliance on fossil fuels remains a challenge mainly due to continued industrialization and urbanization.[1–3] Portland cement (PC) is the most consumed cementitious material in the construction industry, with an approximate production of 4.1 billion tons.[4–6] The cement industry has been estimated to be the third largest contributor (5–8%) to anthropogenic carbon dioxide emissions.[7,8] Most of these emissions (50–60%) are generated by the decomposition of limestone ($CaCO_3$ to CaO), the combustion of fossil fuels in the pyroprocessing unit (30–40%), and electricity consumption.[9] One of the strategies is the replacement of the clinker with supplementary cementituos materials (SCMs). Nevertheless, the clinker replacement fraction is only 25% in all

cements produced globally.[10] Therefore, various alternative binding materials have been developed in recent years. In this context, alkali-activated materials (AAMs) have been considered a viable alternative because of their good mechanical performance and durability, with a low energy demand and environmental impact.[5,11,12] AAMs are obtained from the combination of various raw materials or precursors (*e.g.*, metallurgical slag, fly ash, silica fume, and metakaolin) with an alkaline activator (*e.g.*, MOH, M_2SiO_3, and MOH/M_2SiO_3; M = Na, K), from room temperature to 80–90 °C.[13] Owing to the use of a wide range of precursors and activators, the microstructures and properties of AAMs are diverse, increasing their applications not only as building materials, but also in ceramics, catalysis, foams, coatings, thermal insulators, and in the adsorption of dyes and heavy metals.[14–17] Recently, the application of AAMs, mainly obtained from precursors with low calcium (geopolymers, GPs) content such as, metakaolin (MK), fly ash (FA), and biomass ash, as solid adsorbents for CO_2 capture has attracted significant attention. Several strategies have been proposed to improve their CO_2 adsorption capacity, specifically when combined with zeolites, hydrotalcites, activated carbon or foaming agents.[18–23] However, the synthesis of some of these advanced adsorbents can be expensive and involve complex fabrication processes, limiting large-scale implementation.[24–26] Studies on the preparation of these materials are summarized in Table 1, where it is evident that analytical grade precursors

aInstituto de Ingeniería, Coordinación de Ingeniería Ambiental, Universidad Nacional Autónoma de México, Circuito Exterior S/N, Ciudad Universitaria, Coyoacán, Ciudad de México, 04510, Mexico. E-mail: rramirezz@iingen.unam.mx; Fax: (+52)55 56 23 36 02; Tel: (+52)55 56 23 36 73

bInstituto de Ingeniería, Coordinación de Estructuras, Universidad Nacional Autónoma de México, Circuito Exterior S/N, Ciudad Universitaria, Coyoacán, Ciudad de México, 04510, Mexico

Table 1 Summary of the alkali-activated materials as solid adsorbents for CO_2 capture[a]

AAM or GP	Method of synthesis	Precursor	Other	Compressive strength (MPa)	CO_2 capture capacity (mmol g^{-1})	Ref.
GP-zeolite composite GZ	In situ hydrothermal conversion of geopolymer sphere (90, 120 y 180 °C)	• Municipal solid waste incineration fly ash • Crystal seed ($18Na_2O \cdot Al_2O_3 \cdot 19SiO_2 \cdot 370H_2O$) was prepared using: SH, WG and Al_2O_3	• Coal fly ash (was used as a silica–aluminium additive) • Dimethyl silicone oil at 85 °C to prepare GZS	3.37	0.63	1
Hydrotalcite-rich porous GP	Alkaline activation; In situ generation of Friedel's salts	S105 grade blast furnace slag	• Landfill leachate concentrate • Powder sodium silicate • H_2O_2: F.A. • Humic acid: stabilizer	4.40–4.80	0.22	2, 29
GP and GP-zeolite composite monoliths	Cold sintering process (CSP); Constant pressure of 56 or 168 MPa, for 15 min at 40 °C and for 30 min during cooling	G = potassium-based geopolymer (K-G2) powder (MK as the precursor)	Z = sodium-based geopolymer (Na-G1.2) (81 vol% of the in situ synthetized NaA phase) (MK as the precursor); X = commercial Na13X zeolite powder	4 ± 2–27 ± 2	0.1 bar = 1.1–1.66; 1 bar = 2.16–3.0	3
Metakaolin-based GP – zeolite NaA composites	In situ nucleation of the zeolite NaA	Metakaolin (grade M1200S)	• Commercial zeolite Na4A	Wne	0.1 bar = 1.0; 1 bar = 2.6	30
Foamed and unfoamed GP/NaX zeolite/activated carbon composites (monoliths)	Multiphase reaction–crystallization processes and in situ NaX zeolite gel conversion of metakaolin	Metakaolin	• Activated carbon was prepared from deoiled olive pomace waste	1–16	2.5–3.8	31
In situ synthesis of zeolite X in foam GP (monoliths)	In situ synthesis and hydrothermal conditions	Coal fly ash, classed F	• H_2O_2 and egg protein: F.A. • Commercial zeolite X • H_2O_2 and calcium stearate powder (F.A. and F.S.)	3.0	7.91	32
GP of fly ash and rice husk ash	Alkali-activation	Fly ash; Metakaolin (commercial K 900 °C); Rice husk ash; Rice husk ash calcinated (500 °C)	Not applicable	16.5 (7 days); 11 (28 days)	0.63–0.80	23
Zeolite-fly ash-slag composite porous	Alkali activation	Fly ash, Blast furnace slag (10%)	NaClO solution: F.A. Calcium stearate: F.S. Three different types of zeolite: 13X zeolite, 4A zeolite, and clinoptilolite	6.642–8274 N	1.40–2.68	33
GP based porous composite	Alkali-activation and hydrothermal conditions	Silica fume; Metakaolin	Commercial wooden activated carbon	23.1 (7 days)	1 atm = 60.14 cm^3 g^{-1}	34
Porous alkali-activated fly ash composite	Alkali-activation	High-calcium fly ash	Zinc stearate/H_2O_2 and Al powder (F.A.)	Wne	0.61	21

This journal is © The Royal Society of Chemistry 2025

J. Mater. Chem. A, 2025, 13, 38080–38093 | 38081

Table 1 (Contd.)

AAM or GP	Method of synthesis	Precursor	Other	Compressive strength (MPa)	CO$_2$ capture capacity (mmol g^{-1})	Ref.
GP-hydrotalcite composites (monolites)	Alkali-activation and thermal treatment	Metakaolin grade M1200S	Propylene glycol solution	10–35	0.109–0.145	20
Zeolite-GP composite materials (monolites)	Alkali-activation	Metakaolin grade M1200S	Four commercial HyT samples with different Mg:Al Na13X zeolite powder	3.0	0.1 bar = 0.27–0.29 1 bar = 0.58–1.7	19 35
GP monolite	Alkali-activation	Metakaolin grade M1200S Fumed silica	Not applicable	Wne	0.1 bar = 0.27–0.29 1 bar = 0.57–0.62	18

^{a} GP = geopolymer; Wne = was not valuated; F.A. = foaming agent; F.S. = foam stabilizer; SH = sodium hydroxide; WG = water glass.

and other synthetic materials have been used mainly as raw materials. As can be seen, a wide range of CO$_2$ capture capabilities are shown with compressive strengths varying between 3 and 35 MPa, which are lower than those achieved using specimens produced with MK or FA (35–50 MPa at 28 days).[27,28]

In response to the demand for improved binder sustainability, blast furnace slag (BFS) based AAMs combined with fly ash or metakaolin have emerged as a promising alternative for the production of sustainable construction materials, thanks to their remarkable mechanical strength and durability. Their compressive strength has been the subject of numerous studies, consolidating their potential in the production of concrete and mortar.[36–38] At the same time, carbon dioxide capture and adsorption represent a crucial area for mitigating the environmental impact of the construction industry, which encourages the exploration of materials with dual functionality: mechanical performance and capture of polluting gases. A systematic investigation based on a bibliometric analysis using the open-source software tool VOSviewer shows that research on the integration of both aspects in AAMs is limited (Fig. 1), especially in blast furnace slag-based AAMs. The visualization of networks constructed from the co-occurrence of key terms shows a broad concentration of research focused on their mechanical properties and, separately, on their gas adsorption capacity, with a scarce integration of both lines of research in a single study. In this context, the present study proposes the development of AAMs, prepared with iron slag generated from blast furnace, which simultaneously exhibit high values of compressive strength and CO$_2$ capture capacity. The valuable information explaining the high values of compressive strength and CO$_2$ adsorption will help identify the untapped capabilities of AAMs based on BFS, as well as new research directions and the development of carbon capture applications.

2 Experimental procedure

2.1 Materials and reagents

Iron BFS was used as a precursor for the preparation of AAMs. The BFS was obtained from one of Mexico's leading steel mills (Fig. 2). Sodium silicate and sodium hydroxide were used to prepare an alkaline activator. The activating solution was prepared from a mixture of sodium hydroxide granules (97% purity, Meyer), deionized water (decarbonated), and sodium silicate (14.7% Na$_2$O and 29.5% SiO$_2$ by mass, pH = 12.7, density (20 °C) = 1.53 g cm^{-3}, Silicatos y Derivados S.A de C.V.). Prior to use, the solution was stored under controlled conditions at a temperature of 20 ± 2 °C for 24 h. Alumina (98% purity, calcined, Laboratory BDH Reagent) was used to adjust the Si/Al molar ratio.

2.2 Conditioning and characterization of iron BFS

The BFS was ground in a mill, using steel balls of different diameters, until the particle size was reduced (<38 μm). Once ground, the average particle size was determined using laser granulometry (Mastersizer 2000). The fineness of the particles was measured and represented by the Blaine specific surface or
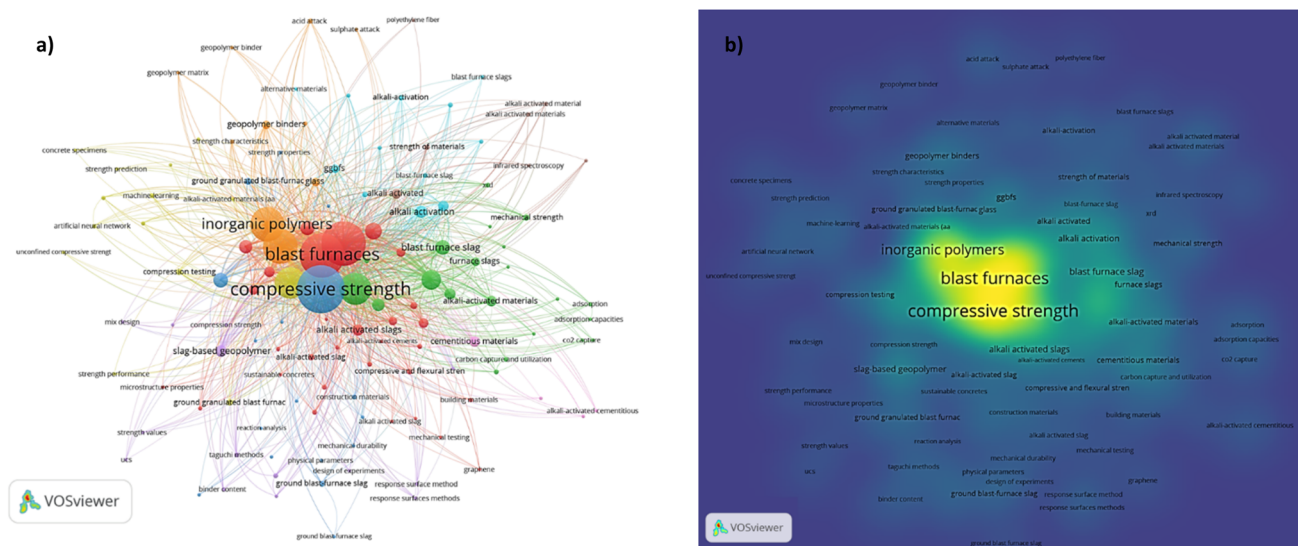
38082 | J. Mater. Chem. A, 2025, 13, 38080–38093

This journal is © The Royal Society of Chemistry 2025

Fig. 1 (a) VOSviewer mapping and (b) density of studies related to alkali-activated blast furnace slag materials, CO_2 capture and compressive strength.

Fig. 2 BFS used in this research study.

Blaine fineness (NMX-C-056-ONNCCE-1997). The chemical composition of the BFS was determined by X-ray fluorescence (XRF) using a Rigaku Primus II analyzer (equipped with a rhodium tube and 125 μm beryllium window). The BFS was characterized by X-ray diffraction (XRD) using an Empyrean Malvern Panalytical diffractometer (nickel filter, Cu K_{α} radiation with $\lambda = 1.5406$ Å, PIXcel3D detector, 5 kV and 40 mA, step size of 0.002°, and an integration time of 50 s per step). The morphology of the BFS particles was observed by scanning electron microscopy (SEM) using a Philips XL20 microscope with a 25 kV backscattered electron (BSE) detector and a working distance of 4 mm.

2.3 Preparation of AAM specimens

The design of experiments (DOE) methodology was followed to obtain the AAM with the highest compressive strength and to evaluate its CO_2 capture capacity. The factors studied in the preparation of AAMs by alkaline activation of BFS with

a mixture of NaOH/Na$_2$SiO$_3$ were the Ms modulus (SiO$_2$/Na$_2$O mass ratio), Si/Al molar ratio, and liquid/solid mass ratio (L/S). In particular, the study range of the SiO$_2$/Na$_2$O ratio, from 0.5 to 1.5, was employed based on previous research, in which the influence of the SiO$_2$/Na$_2$O ratio (0.2–3.0) on the compressive and flexural strength and porosity has been studied.[39–43] The results have shown that in the range between 0.5 and 2.0, in combination with other factors (Na$_2$O content, NaOH concentration, curing conditions, and liquid/solid ratio), microstructural integrity, homogeneity, mechanical properties, and durability of the materials perform optimally. This is due to the rapid and continuous dissolution of the precursor, which favors the formation of greater amounts of reaction products (gels). The compressive strength was used as the response factor (7 and 28 days). The studied factors and levels were chosen based on the work described by Wang and Scrivener (1995); Fernández-Jimenez and Puertas (1997); Puertas and Torres-Carrasco (2014).[44–46] The experiments were designed using a 3^K response surface procedure with $K = 3$ factors, 27 model points, one center point, and one replica. The factors and their levels are listed in Table 2. The input parameters of the model points were randomly generated using Statgraphics Centurion XVI software (SI).

The AAM specimens were prepared by mixing the ground BFS, calcined alumina, and activating solution in a mixer (Worner Beixi JJ-5) at 80 rpm for 5 min. The paste obtained was poured

Table 2 Range of each factor used in the experimental design

| Factor | Symbol | Coded variable level | | |
		−1	0	1
SiO$_2$/Na$_2$O ratio	A	0.5	1.0	1.5
L/S ratio	B	0.4	0.5	0.6
Si/Al ratio	C	2.0	2.5	3.0

This journal is © The Royal Society of Chemistry 2025

J. Mater. Chem. A, 2025, **13**, 38080–38093 | **38083**

Fig. 3 Specimen used for the compressive strength test.

into cylindrical plastic molds with a height to diameter ratio of 2 (Φ13 mm, $h = 26$ mm), and were vibrated for 10 min in a vortex (Glas-Col Multi-Pulse Vortex). Subsequently, the specimens obtained (Fig. 3) were cured for 7 and 28 days at constant temperature (22 $\pm$ 2 °C) and relative humidity (98 $\pm$ 3%) in a conventional curing chamber. Compressive strength tests were performed in triplicate according to ASTM C39 on a universal MTS 20T machine with a preload of 3 kg and a displacement load at a constant rate of 5 mm min^{-1}. The compressive strength of the AAMs was expressed as the average value of the three measurements after 7 and 28 days of curing (most common normative and informative ages). After testing, the resulting fragments were washed with 80 mL of an acetone/ethanol mixture (1 : 1 by volume) and dried at 120 °C for 24 h to stop hydration/activation reactions.[47] Finally, the fragments were placed in a desiccator under vacuum until the CO_2 capture capacity was evaluated and microstructural characterization was conducted.

2.4 CO_2 capture tests

The capture capacity of the AAMs was determined by the CO_2 adsorption of the specimens with the highest compressive strength at 7 and 28 days. Additionally, to determine the influence of the Ms modulus and Si/Al molar ratio, specimens with different Ms moduli and Si/Al ratios were selected, keeping the L/S ratio at its optimal value (obtained from the DOE analysis). To determine the CO_2 adsorption capacity, a thermogravimetric analyzer (Labsys Evo Setaram Thermobalance) was used to record the mass gain during the adsorption process. One of the fragments obtained after the compressive strength tests (60–80 mg) was placed in an alumina crucible. The analysis program included a flow pretreatment of N_2 (40 mL min^{-1}, grade 4.7) at 200 °C for 2 h with a heating rate of 10 °C min^{-1} to remove any species adsorbed on the surface and subsequent cooling to 35 °C for 20 min to obtain stable conditions. The gas was then changed from N_2 to CO_2 to start the adsorption process at 35 °C under 20%

Table 3 Chemical composition of BFS

SiO_2[a]	39.1
Al_2O_3	12.0
CaO	32.9
MgO	10.2
TiO_2	1.6
Fe_2O_3	1.6
MnO	1.4
Na_2O	0.9
K_2O	0.1
L.O.I[b]	0.2
Total	100.0

[a] Weight percent. [b] L.O.I = Loss on ignition.

CO_2 flow (N_2 balance, certified standard) at 60 mL min^{-1} for 4 h. Three fragments were analyzed for each selected AAM. The capture capacity of the AAMs was expressed as the average value of the three analyzed fragments.

2.5 Microstructural characterization

The specific surface and pore volume of the selected AAMs were determined from the N_2 adsorption–desorption isotherm at 77 K, using a BelSorp Mini II (Bel-Japan). The specific surface area was calculated using the Brunauer–Emmett–Teller (BET) method, and the pore size distribution was calculated from the desorption data using the Barrett–Joyner–Halenda (BJH) method. Fourier transform infrared spectroscopy (FTIR) from 4000 to 400 cm^{-1} was conducted on a Thermo Scientific Nicolet 6700 spectrometer, equipped with a total attenuated reflectance (ATR) unit with a resolution of 2 cm^{-1} and 64 scans. Five different points were analyzed for each specimen. The morphological and microstructural characteristics of the selected AAMs were examined by SEM under a Philips XL20 microscope.

3 Results and discussion

3.1 Characterization of BFS

The results of the XRF analysis (Table 3) indicate that BFS was mainly composed of silicon, calcium, aluminum, and magnesium oxides, which constituted 94.2% of the overall composition.
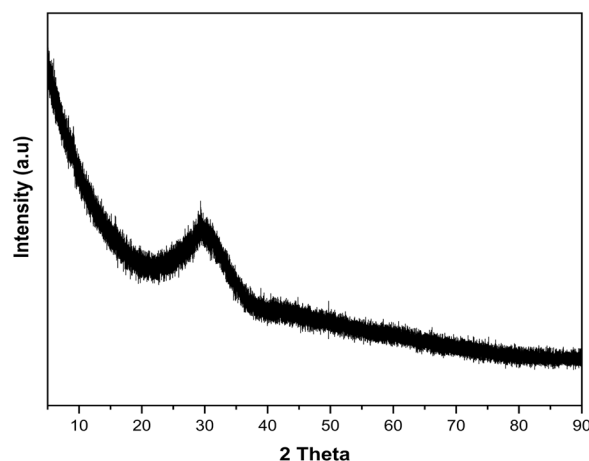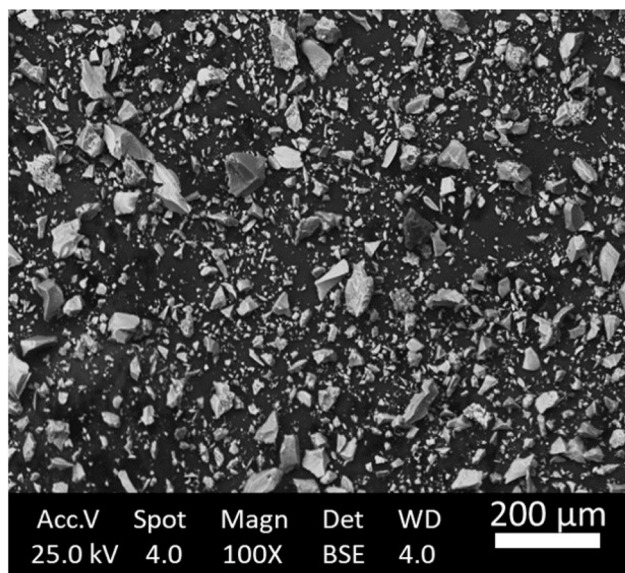

Fig. 4 XRD pattern of BFS.

38084 | J. Mater. Chem. A, 2025, 13, 38080–38093

This journal is © The Royal Society of Chemistry 2025

Fig. 5 Backscattered electron image of BFS.

The XRD pattern corroborated its vitreous nature, identified by background lifting and the presence of a wide halo over 25–35° of 2θ (Fig. 4).
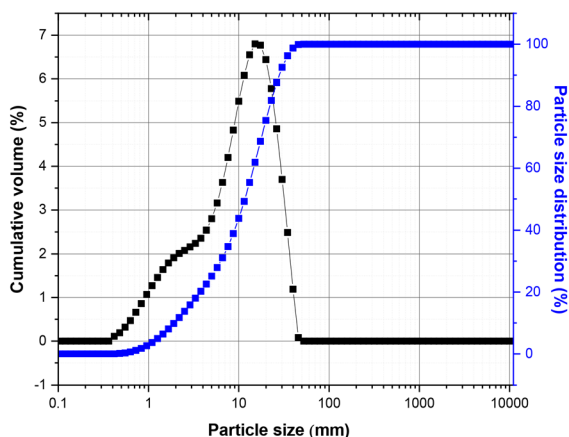

Fig. 6 Cumulative volume and size distribution of BFS.

The morphology of the BFS particles is presented in Fig. 5, which shows that the slag was composed of irregularly shaped and angular particles. Fig. 6 shows the particle size distribution of the BFS after grinding. The mean particle size was 11.7 μm (D_{50}), with a Blaine specific surface of 527 m^2 kg^{-1}. The particle size distribution indicated that 90% of the particles had sizes of less than 27.8 μm and 10% had a particle size of less than 1.9 μm.

3.2 Characterization of AAMs

3.2.1 Compressive strength. The AAMs exhibited compressive strengths of 1.9–70.0 MPa and 4.3–84.0 MPa at 7 and 28 days, respectively. As noted, the compressive strength varies over a wide range depending on the alkaline activation conditions of the BFS. It is known that compressive strength depends on several factors, such as the characteristics of the precursor, type of activator, and curing conditions.[16,48–50] These factors determine the dissolution kinetics of the precursor and polycondensation reactions, and therefore define the final properties of AAMs.[48] Analyses of the variance indicated that the three factors studied had a significant effect on the compressive strength of the AAMs. The optimization of the factors through the desirability function allowed a maximum resistance of 71.5 MPa and 88.3 MPa at 7 and 28 days, respectively, to be achieved when setting the factors at 1.5 for the SiO_2/Na_2O mass ratio, 0.4 for the liquid/solid mass ratio, and 3.0 for the Si/Al molar ratio ($AAM_{1.5,\ 0.4,\ 3.0}$, subscripts denote Ms moduli, L/S and Si/Al, respectively). Regarding the conditions for alkaline activation of BFS, it was found that the factors studied and their optimal values are within the ranges reported previously, with compressive strength values between 70 and 100 MPa.[44,45,51,52] Table 4 shows the CO_2 capture capacity of the AAMs ($AAM_{1.5,\ 0.4,\ 3.0}$) obtained under optimal conditions, which exhibited the highest compressive strength at 7 and 28 days. AAMs with different Ms moduli (1.0 and 0.5) and Si/Al molar ratios (2.5 and 2.0), with the liquid/solid mass ratio fixed at the optimal value (L/S = 0.4), were used to evaluate the effect of these two parameters on its CO_2 capture capacity.

3.2.2 Microstructure and textural properties. Fig. 7 shows micrographs obtained during the SEM characterization of the AAMs, in which a compact morphology was observed,

Table 4 Samples of selected AAMs and the corresponding CO_2 capture capacity

Sample	Experimental conditions			Compressive strength (MPa)				CO_2 capture (mmol g^{-1})			
	Ms	L/S	Si/Al	7 days	$\sigma_s{}^a$	28 days	$\sigma_s{}^a$	7 days	$\sigma_s{}^a$	28 days	$\sigma_s{}^a$
$AAM_{1.5,\ 0.4,\ 3.0}$	1.5	0.4	3.0	71.5	1.4	88.3	1.5	0.34	0.02	0.26	0.01
$AAM_{1.0,\ 0.4,\ 3.0}$	1.0	0.4	3.0	56.7	0.7	67.7	0.2	0.64	0.01	0.59	0.01
$AAM_{0.5,\ 0.4,\ 3.0}$	0.5	0.4	3.0	44.2	1.2	59.5	2.4	0.71	0.01	0.67	0.02
$AAM_{0.5,\ 0.4,\ 2.5}$	0.5	0.4	2.5	39.4	0.6	52.1	1.9	0.77	0.01	0.72	0.01
$AAM_{0.5,\ 0.4,\ 2.0}$	0.5	0.4	2.0	35.6	0.7	46.5	0.6	0.80	0.01	0.76	0.01

^{a} The standard deviation was evaluated using the formula of common standard deviation $\left(\sigma = \sqrt{\dfrac{1}{N}\sum_{i=1}^{n}(X_i - \mu)^2}\right)$, where σ is the standard deviation of the values, N is the number of samples to be measured in each group, X_i is the value of a sample measured at the ith time, and μ is the average value from X_1 to X_N.
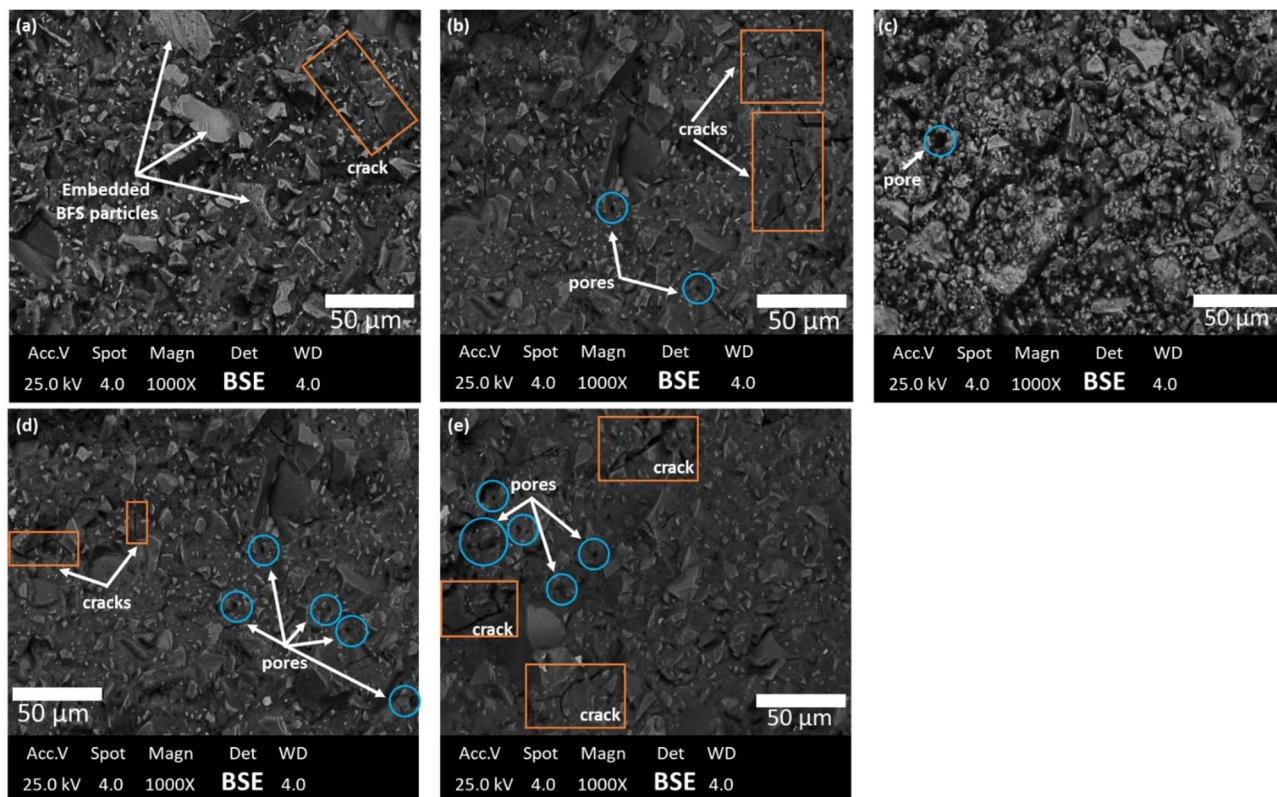
Fig. 7 Backscattered electron image of (a) $AAM_{1.5,\ 0.4,\ 3.0}$, (b) $AAM_{1.0,\ 0.4,\ 3.0}$, (c) $AAM_{0.5,\ 0.4,\ 3.0}$, (d) $AAM_{0.5,\ 0.4,\ 2.5}$, and (e) $AAM_{0.5,\ 0.4,\ 2.0}$.

consisting of BFS particles embedded in the matrix and/or partially dissolved as well as small pores and cracks. The AAMs which exhibited lower mechanical resistance ($AAM_{0.5,\ 0.4,\ 2.5}$ and $AAM_{0.5,\ 0.4,\ 2.0}$) were observed to have a greater number of pores and crack. These characteristics are important because they can influence the mechanical and adsorption properties of AAMs.[53] The results suggest that the presence of slag particles in the matrix could be beneficial for the mechanical properties of the AAMs. Zhang *et al.*[54] studied the influence of blast furnace slag on the rheological,

mechanical, and reaction kinetics and porosity properties of geopolymers obtained from recycled concrete. Their results indicated that the addition of slag in proportions greater than 30% by weight accelerates the setting process and significantly improves mechanical properties, exhibiting compressive strengths of 61.2 MPa and flexural strengths of 5.17 MPa. This increase was attributed to both the morphology and the reactivity of the slag itself. The irregular and angular shape of the particles increases the shear stress in the geopolymer paste due to greater friction between the particles, which favors contact
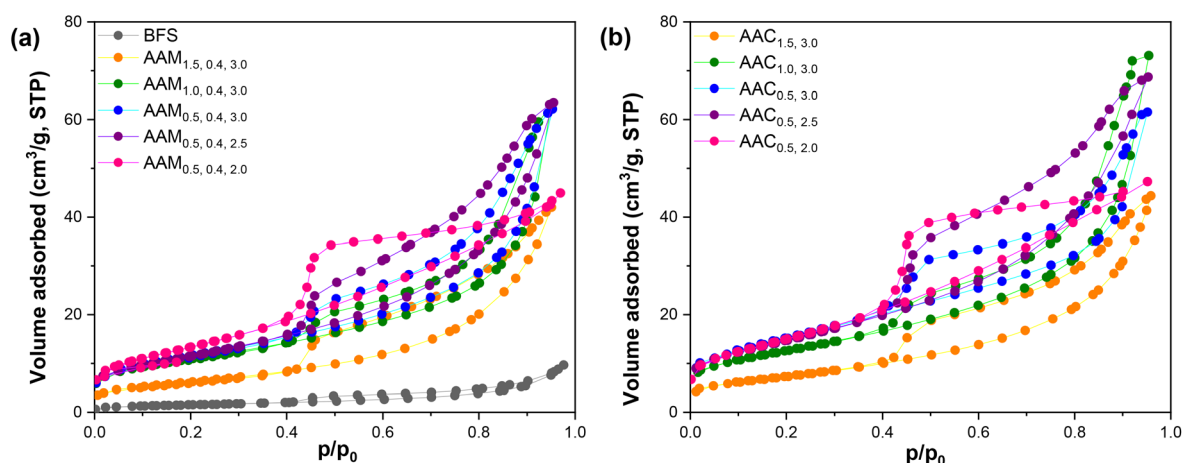

Fig. 8 Nitrogen adsorption–desorption isotherms of AAMs at (a) 7 and (b) 28 days.

38086 | *J. Mater. Chem. A*, 2025, **13**, 38080–38093

This journal is © The Royal Society of Chemistry 2025

between the solids and the alkaline activator, obtaining greater formation of C–A–S–H and C–S–H gels, and consequently, greater mechanical resistance (favoring the reaction). Furthermore, the increase in friction and adhesion between particles increases the elastic limit and plastic viscosity of the geopolymer. It is worth noting that the presence of CaO, together with the rough and angular structure of the slag particles, influences the setting time, significantly accelerating it. On the other hand, Alzaza et al.[55] demonstrated that the angularity and roughness of granulated blast furnace slag (BFS) particles increase the initial compressive strength of PC/GBFS mortars when used as fine aggregates (20–50%), in addition to improving resistance to freeze–thaw cycles and sulfuric acid attack. Wang et al.[56] documented that the angular shape of steel slag particles positively impacts the strength and durability of concrete when used as a fine aggregate. This suggests that the morphology of blast furnace slag particles plays a fundamental role in the development of the mechanical properties of AAMs. In addition, the cracks and insulated pores on the surface are attributed to the evaporation of water and contraction of the material during the curing process.[57] The N_2 adsorption–desorption isotherms of BFS and AAMs at 7 and 28 days are presented in Fig. 8.

In the case of BFS, the curve corresponds to a type II isotherm with a type H3 narrow hysteresis loop, according to the IUPAC classification,[58] which is typical of non-porous solids. AAMs at 7 and 28 days displayed type IV isotherms with increments at a pressure close to zero ($p/p_0 = 0$–0.1) and a type H3 hysteresis loop at high pressure ($p/p_0 = 0.4$–1.0), indicating the limited presence of mesopores and micropores. This is common in solids composed of aggregates or agglomerates of

particles.[59] The shapes of the isotherms suggest similar porosities; however, their textural parameters may vary.[60] Table 5 lists the specific surface area (BET method) values. This area mainly corresponds to the surface of the mesopores.[61,62] In this case, BFS has a lower surface area (5.5 $m^2 g^{-1}$) than AAMs, which have areas of 22.1–49.3 $m^2 g^{-1}$ and 26.4–55.8 $m^2 g^{-1}$ at 7 and 28 days, respectively. Compared with other AAMs, similar and even higher BET area values were evident (Table 5).

However, the surface area values suggest that there is no relationship between the BET surface area and CO_2 capture capacity. If we consider the Si/Al molar ratio of the studied AAMs, it is possible to observe an increase in the CO_2 capture capacity as the Si/Al ratio decreases (Table 4). According to, Freire et al.[23] a lower Si/Al atomic ratio supposes an increase in the hydrophilic character and a higher number of basic Lewis sites, which also explains the observed behavior, favoring the adsorption capacity for CO_2 of the AAMs. Properties such as compressive strength, permeability, diffusivity, and shrinkage are closely related to pore size distribution, pore volume, and porosity.[63] These characteristics directly depend on the curing conditions and chemical composition of the matrix.[21,63] The pore size distributions (PSDs) obtained by the BJH method for the AAMs are presented in Fig. 9. It shows that the pore sizes were largely less than 20 nm. AAMs have a mesoporous structure characterized by the presence of 1–3 nm pores. The presence of micropores between 1 and 2 nm has been considered suitable to improve the CO_2 capture by adsorbent materials under environmental conditions because adsorption takes place mainly in the narrow pores since the kinetic diameter of CO_2 is 0.33 nm.[64]

Table 5 Pore volume and BET specific surface area of AAMs and BFS[a]

AAM or GP	S_{BET} ($m^2 g^{-1}$)	Pore volume ($cm^3 g^{-1}$)	Reference
GP-zeolite composite (GZ)	252	0.540	1
Hydrotalcite-rich porous GP	—	0.041	2
GP and GP-zeolite composite monolites	233–310	0.338–0.385	3
GP of fly ash and rice husk ash	8.8–20.9	0.036–0.060	23
Zeolite-fly ash-slag composite porous	239–388	0.461–0.837	33
GP based porous composite	256 (ACGZ)	0.33 (ACGZ)	34
	25 (GZ)	0.088 (GZ)	
Porous alkali-activated fly ash composite	8.4–35.9	0.03–0.17	21
GP-hydrotalcite composites (monolites)	32–56	—	20
Zeolite-GP composite materials (monolites)	161–211	0.302–0.475	19
	3–88 (GP)	0.254–0.339 (GP)	35
GP monolite	22.0–31.9	0.140–0.360	18
BFS	5.5	0.02	This work
AAM$_{1.5, 0.4, 3.0}$ (7 days)	22.1	0.073	
AAM$_{1.0, 0.4, 3.0}$	36.9	0.078	
AAM$_{0.5, 0.4, 3.0}$	39.9	0.100	
AAM$_{0.5, 0.4, 2.5}$	40.9	0.110	
AAM$_{0.5, 0.4, 2.0}$	49.3	0.120	
AAM$_{1.5, 0.4, 3.0}$ (28 days)	26.4	0.065	
AAM$_{1.0, 0.4, 3.0}$	43.3	0.096	
AAM$_{0.5, 0.4, 3.0}$	52.9	0.098	
AAM$_{0.5, 0.4, 2.5}$	53.1	0.098	
AAM$_{0.5, 0.4, 2.0}$	55.8	0.100	

[a] GZ = geopolymer-zeolite composite; ACGZ = activated carbon geopolymer-zeolite composite; GP = geopolymer.

This journal is © The Royal Society of Chemistry 2025

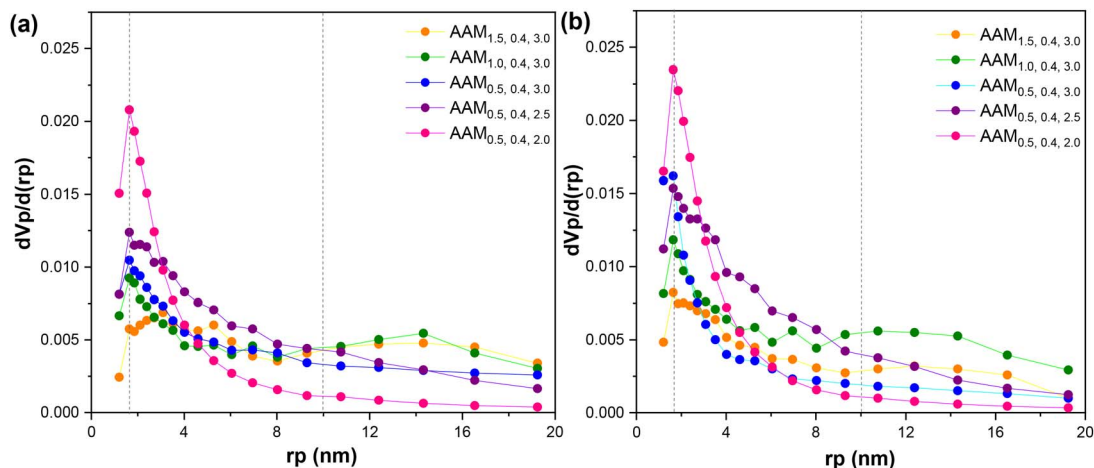J. Mater. Chem. A, 2025, **13**, 38080–38093 | **38087**

Fig. 9 PSD curves of AAMs after (a) 7 and (b) 28 days.

The PSD curves indicate that the AAMs possessed a homogeneous mesoporous structure characterized by a pore size distribution centered at 1–3 nm, which constitutes the main structure of the AAMs with the highest CO_2 capture capacity ($AAM_{0.5, 0.4, 3.0}$, $AAM_{0.5, 0.4, 2.5}$ and $AAM_{0.5, 0.4, 2.0}$). In contrast, AAMs with lower capture capacities have a heterogeneous pore size distribution, indicating the presence of larger pores (10–16 nm). Table 5 shows the values of the two textural properties of AAMs, which indicate that pore volumes were within the range observed for other alkali-activated materials that have been previously evaluated for CO_2 capture. These values show an increase in the total pore volume as the SiO_2/Na_2O mass ratio decreases from 1.5 to 0.5, as well as a decrease in the Si/Al molar ratio from 3.0 to 2.0, suggesting that the increase in adsorption capacity is related to pore volume. The PSD curves also show important changes in this parameter as the SiO_2/Na_2O and Si/Al ratios decreased from a bimodal distribution (wide and heterogeneous) to a unimodal distribution. This indicated that an increase in pore volume, the presence of micropores (1–3 nm), and a structure comprised mostly of homogeneously distributed mesopores, enable greater CO_2 capture capacity by the AAMs.

3.3 CO_2 adsorption analysis of AAMs

Fig. 10 shows the CO_2 adsorption profiles as a function of time. The profiles suggest rapid adsorption of CO_2 for $AAM_{0.5, 0.4, 3.0}$, $AAM_{0.5, 0.4, 2.5}$, and $AAM_{0.5, 0.4, 2.0}$, which is related to the high mobility of sodium ions in the network and/or the organization of pores in the polymer network.[65] The maximum adsorption of CO_2 for each AAM is presented in Table 6, along with the values observed for other materials reported in the literature. The AAMs prepared in this study had a capture capacity of 0.34–0.80 mmol g^{-1} and 0.26–0.76 mmol g^{-1} after 7 and 28 days, respectively. These values indicate that these AAMs exhibited a capture capacity similar to and even higher than those reported for other materials obtained by alkaline activation. These other materials require a combination with zeolites, hydrotalcites, or foaming agents, which are commonly used to

capture CO_2 and increase their capture capacity. The values obtained suggest that an increase in the amount of sodium and alumina in the reaction medium, as a consequence of the decrease in the Si/Al molar ratio and the SiO_2/Na_2O mass ratio, increases the CO_2 capture capacity. This is due to the significant effect of these factors on the pore structure of the AAMs, promoting the formation of micro- and mesopores. The Si/Al molar ratio is an important parameter that determines the stability of the network through the different tetrahedral
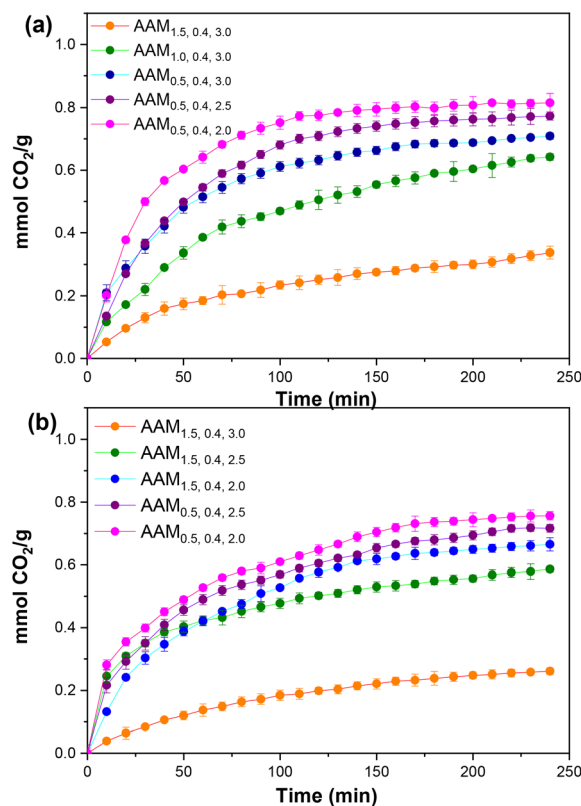

Fig. 10 CO_2 uptake profiles of AAMs at (a) 7 and (b) 28 days (error bars are standard errors).

38088 | J. Mater. Chem. A, 2025, 13, 38080–38093

This journal is © The Royal Society of Chemistry 2025

Table 6 CO_2 adsorption capacities reported in the literature for several materials and the AAMs prepared in this work[a]

AAM or GP	Method and adsorption conditions	Compressive strength (MPa)	CO_2 capture capacity (mmol g^{-1})	Reference
GP-zeolite composite GZ	Fixed-bed reactor 25 °C, 1 atm	3.37 MPa	0.63	1
Hydrotalcite-rich porous GP	Thermogravimetric analyzer and a gas adsorption analyzer 35 °C y 200 °C	4.40–4.80 MPa	0.22	2 and 29
GP and GP-zeolite composite monoliths	Volumetric technique 35 °C, 0.1 y 1 bar	4±2–4.6 MPa	0.1 bar = 1.1–1.66 1 bar = 2.16–3.00	3
Amine functionalized porous GP spheres	Fixed-bed reactor 35, 50, 65 and 80 °C	Wne	2.55 (65 °C) 0.86 (35 °C)	77
Metakaolin-based geopolymer-zeolite NaA composites	Volumetric method 35 °C, 0.1 y 1 bar	Wne	0.1 bar = 1.0 1 bar = 2.6	78
Foamed and unfoamed GP/NaX zeolite/activated carbon composites (monolites)	Volumetric method (Sieverts' type apparatus) 0.1–1 bar, 298 K	1–16	2.5–3.8	31
In situ synthesis of zeolite X in foam GP	Physisorption analysis Dynamic adsorption experiments	3	7.91	32
GP of fly ash and rice husk ash	Thermogravimetric method 35 °C, 1 bar	16.5 (7 days) 11 (28 days)	0.63–0.80	23
Zeolite-fly ash-slag composite porous	Dynamic and static method 25 °C, 0.1 MPa	6.642–8274 N	1.4–2.68	33
GP based porous composite	Physisorption analysis 0–1 atm, 35 °C	23.1 (7 days) (ACGZ) 35.2 (GZ)	1 atm = 60.14 cm³ per g (AGZ) 1 atm = 4.40 cm³ per g (GZ)	34
Porous alkali-activated fly ash composite	25 °C, 0–1 atm	Wne	0.61	21
GP-hydrotalcite composites (monolites)	Physisorption analysis 200 °C	10–35	0.109–0.145	20
Zeolite-GP composite materials (monolites)	Thermogravimetric method 35 °C, 0.1 y 1 bar 20% CO_2–N_2 gas mixture	3	0.1 bar = 0.59–1.1 1 bar = 1.1–2.5 0.1 bar = 0.27–0.6 1 bar = 0.58–1.7 (GP)	19 and 35
GP monolite	Volumetric method 35 °C, 0–1 bar	Wne	0.1 bar = 0.27–0.29 1 bar = 0.57–0.62	18
AAMs (AAM$_{0.5,\ 0.4,\ 2.0}$)	Thermogravimetric method 35 °C, P_{CO_2} = 0.2	35.6 (7 days) 46.5 (28 days)	0.80 0.76	This work

[a] GZ = geopolymer-zeolite composite; ACGZ = activated carbon geopolymer-zeolite composite; GP = geopolymer; Wne = was not evaluated, P_{CO_2} = partial pressure of CO_2.

connection modes of $[SiO_4]^{4-}$ and $[AlO_4]^{5-}$. When the Si/Al molar ratio is low, most $[SiO_4]^{4-}$ are connected to $[AlO_4]^{5-}$ by sharing a bridge oxygen, according to Lowestein's rule, modifying the pore structure.[6,66] In general, the Si/Al ratio influences the microstructure and is one of the most critical relationships as it affects gel formation, and determines the structural reorganization and densification of geopolymers.[67] Wang *et al.*[27] determined that a Si/Al ratio of 1.5 generates a smaller pore volume (0.017 cm³ g^{-1}) and pore size (6.21 nm), compared to a higher Si/Al ratio (2.5), decreasing the degree of efflorescence of the geopolymers. On the other hand, Freire *et al.*[23] observed an increase in CO_2 capture capacity when analyzing the Si/Al ratio of geopolymers by XPS, as the Si/Al ratio decreases from 4.02 to 2.84, due to an increase in hydrophilic character and a greater number of basic Lewis sites. Kamseu *et al.*[68] found that pore morphology is a parameter that depends on the Si/Al

relationship. Degefu *et al.*[67] observed that the porosity of metakaolinite geopolymers increased on decreasing the Si/Al ratio, from 3 to 1.8. They also observed a variation in the pore volume distribution with the Si/Al ratio, finding that the proportion of pores in the gel increases with the increase in the Si/Al ratio. It is important to consider that not only the Si/Al ratio modifies these properties.[69] In the case of zeolites, it has been found that the Si/Al ratio affects the CO_2 adsorption capacity, where a lower Si/Al ratio increases its capture capacity.[70] Other authors have observed that an increase in the Si/Al ratio leads to a decrease in the surface area, attributed to the collapse of pores in the zeolite.[71] Therefore, these studies indicate that the Si/Al ratios should be kept below 2 to increase their capture capacity. Thus, the Si/Al ratio is also an important parameter. The adsorption of CO_2 in AAMs has been explained through two main mechanisms. Due to the substitution of Si for

This journal is © The Royal Society of Chemistry 2025

J. Mater. Chem. A, 2025, **13**, 38080–38093 | **38089**

Al, the structure is electronegative, which favors the physical adsorption of CO_2, similar to that of zeolites.[72] The presence of Si–OH and Al–OH (3400–3000 cm^{-1}) active sites on the surface of the AAM favors chemical adsorption by forming chemical or hydrogen bonds with CO_2.[18] However, for an understanding of the adsorption mechanism in iron slag-based AAMs, a more in-depth study is required. For example, Wang et al.[1] based on adsorption energy calculations of the state density and differential charge density using DFT, have further evaluated the interactions between the geopolymer-zeolite composite and CO_2. The alkaline nature of the surface of AAMs is another important factor for their adsorption capacity because carbon dioxide is an acidic gas that has a strong affinity for alkaline sites or surfaces.[73] Some authors have observed a relationship between the CO_2 adsorption capacity and the concentration of basic sites accessible on the surface of these materials.[23,73–76] Thus, the SiO_2/Na_2O mass ratio (Ms modulus) and Si/Al molar ratio determine the composition and microstructure of the gel and, therefore, its ability to capture CO_2

Previous studies have shown that these types of materials exhibit different capture capabilities because of their microstructure and intrinsic porosity, which depend on the activation conditions and curing process.[63,76,79] Additionally, the AAMs with the CO_2 capture capacities presented in this study ($AAM_{0.5, 0.4, 3.0}$, $AAM_{0.5, 0.4, 2.5}$, and $AAM_{0.5, 0.4, 2.0}$) also had high compressive strengths (35.6–44.2 MPa and 40.5–63.5 MPa at 7 and 28 days, respectively), as compared to other activated alkali materials that have been evaluated as solids for CO_2 capture with compressive strengths less than 16–23 MPa and 11 MPa after 7 and 28 days, respectively (Table 6). This suggests that the microstructure and homogeneous pore distribution contribute to the excellent compressive strengths observed. These results indicate that the AAMs obtained in this study from the activation of BFS with $NaOH/Na_2SiO_3$ have great potential for use in the construction industry because they display excellent compressive strength values and have a high CO_2 capture capacity. The results showed a decrease in the CO_2 capture capacity of the AAMs after 28 days, owing to a lower pore volume (Table 5). The decrease in pore volume was attributed to changes in the microstructure during the curing process. A long curing period allows for complete polymerization, leading to the progress of the network, which is reflected in the densification of the microstructure and an increase in compressive strength.[80] The shape of the PSD curves of the AAMs remained unchanged, and only a small reduction in the volume of mesopores (10–18 nm), which does not compromise their adsorption capacity, was observed (Fig. 9b). AAMs exhibited a decrease in their ability to capture CO_2 (0.80 and 0.76 mmol g^{-1}); however this decrease was not significant and compared with other materials reported in the literature (Table 6).

3.4 Fourier transform infrared spectroscopy (FTIR) analysis of AAMs

Fig. 11 presents the FTIR spectra of the AAMs (7 days of curing) before and after the CO_2 capture process. The spectra show changes in BFS after alkaline activation (Fig. 11a). The FTIR
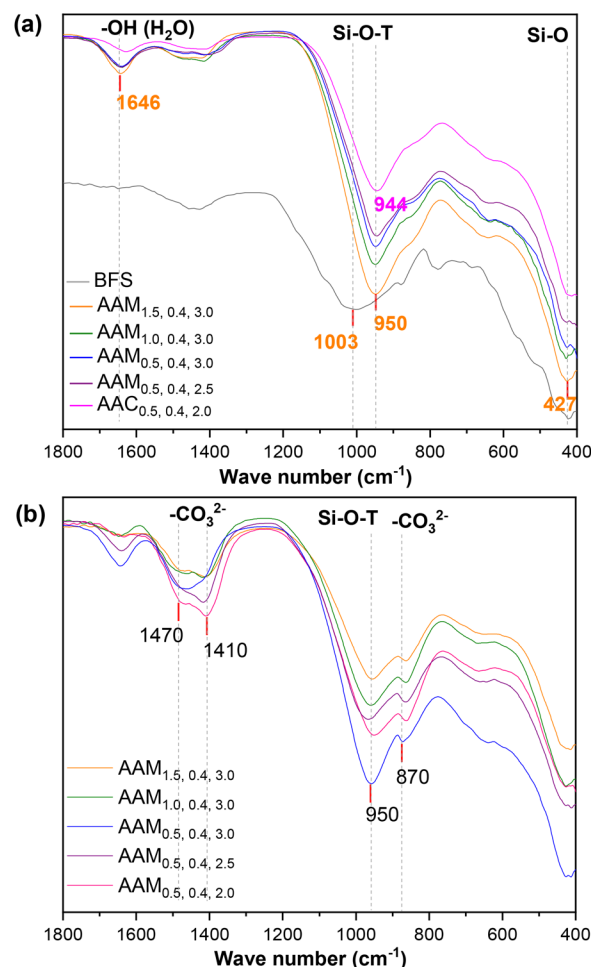

Fig. 11 FTIR spectra of BFS and AAMs (a) before and (b) after CO_2 uptake.

spectrum of the BFS shows a wide and intense band at 1003 cm^{-1} that corresponds to the asymmetric stretching vibration of the Si–O–T bond (T = Si, Al). The displacement of this band to lower wavenumbers (950–944 cm^{-1}) indicates the formation of a new Si–O–T bond from the reaction of the vitreous component present in the BFS with the alkaline activator to form the aluminosilicate gel.[81] This band is characteristic of AAMs and determines the degree of polymerization, indicating the incorporation of Al into the network (Si–O–Si → Si–O–Al). Therefore, with an increase in the content of Al^{3+}, a shift to lower wavenumbers is observed.[82–84] The stretching and bending vibrations of the Si–O bond were observed at 670–660 cm^{-1} and 460–420 cm^{-1}, respectively.[27] The presence of water in the structure of the AAMs was corroborated by the band located at 1650–1640 cm^{-1}, corresponding to the bending mode of –OH, as well as a broad band in the region between 3350 and 3320 cm^{-1}, which is attributed to surface –OH groups of Si–OH.[52,85] After the capture process (Fig. 11b), the spectra of the AAMs displayed new bands at 1470–1450 cm^{-1}, 1410–1400 cm^{-1} and 870–863 cm^{-1}. The bands at 1470–1450 cm^{-1} and 1410–1390 cm^{-1} correspond to the asymmetrical stretching of the O–C–O bond (CO_3^{2-}), which suggests the presence of different

38090 | J. Mater. Chem. A, 2025, 13, 38080–38093

This journal is © The Royal Society of Chemistry 2025

types of carbonates.[86,87] Specifically, the band at 1410–1390 cm^{-1} is characteristic of sodium carbonate.[88] The band at 870–863 cm^{-1} is due to the in-plane bending vibration of the C–O bond (CO_3^{2-}). The presence of these bands has been linked to the adsorption of CO_2 on the surface of AAMs.[21] The increase in the intensity of the signals owing to the vibration modes of carbonate indicates a higher concentration of carbonate, which is related to a greater CO_2 capture capacity. Conventional adsorbents such as activated carbon, zeolites, graphene, and metal–organic frameworks (MOFs) have been widely recognized for CO_2 capture,[89] each with particular advantages and limitations.

Zeolites, for example, have limited adsorption capacity at temperatures above 200 °C and low selectivity towards N_2 and H_2O.[90–93] MOFs offer high adsorption capacity at high pressures; however, they present problems of structural instability and limitations related to the synthesis method (cost, non-eco-friendly, and complex).[94] Recently, alkali-activated materials have emerged as an alternative for CO_2 capture, with capacities below 1.0 mmol g^{-1}. However, it has been observed that their performance improves with the incorporation of other materials such as activated carbon, zeolites, and hydrotalcites. The AAMs based on BFS with developed in this work, with a capture capacity of 0.80 mmol g^{-1}; although its capture capacity compared to MOFs or zeolites, are comparable to and even superior to that of other AAMs or composite materials under hydrothermal conditions and with the addition of seed crystals,[1] the use of foaming and stabilizing agents,[2] the inclusion of commercial zeolites[3,30,31,33] and amines,[77] or the use of polyethylene glycol and washing and calcination processes[21,77] were required for the synthesis of the adsorbent materials. In general, the properties of AAMs depend on several factors, such as the type of precursor and activator (Si/Al, SiO_2/Na_2O, liquid/solid) and the curing conditions (temperature, time, and humidity).[21,44–46] The inclusion of other materials also directly influences their properties. Li et al.[33] observed that the incorporation of various zeolites increased the adsorption capacity from 0.83 to 2.68 mmol g^{-1}, although with a reduction in their mechanical strength and an increase in their cost. Synthetic zeolites have been estimated to have costs ranging from $3.82 to 6.36 USD per kilogram,[29] MOFs between $10 and $30 USD,[95] while activated carbon and other carbon compounds range from $1.06 to $1.34 USD per kilogram.[96] Therefore, AAMs obtained from iron blast furnace slag are emerging as a promising alternative for sustainable CO_2 capture, since they are obtained by utilizing the slag using a simple process and with an adequate balance between adsorption capacity and mechanical strength. These properties also offer advantages in relation to their operational efficiency and cost reduction (column adsorption processes). Therefore, the results obtained serve as a reference point for optimizing their properties (porosity and density) and implementing methodologies that enhance their adsorption capacity.

4 Conclusions

AAMs with high compressive strengths and different CO_2 capture capacities were prepared using BFS and calcined alumina. The AAMs prepared under optimal experimental conditions showed a CO_2 capture capacity of 0.80 mmol g^{-1} and 0.76 mmol g^{-1} (35 °C, $P_{CO_2} = 0.2$) and compressive strengths of 35.6 MPa and 40.5 MPa at 7 and 28 days, respectively. The values of compressive strength are equal to and even higher than those reported for materials prepared from the combination of a precursor (analytical grade metakaolin) and other adsorbents commonly used in the capture of CO_2 (zeolites, hydrotalcites, and activated carbon). The adsorption capacities were strongly influenced by the alkaline nature of the solid surface, as determined by the SiO_2/Na_2O mass ratio, and to a lesser extent, by the specific surface area. The microstructure consisted mostly of mesopores, as well as the presence of micropores between 1 and 3 nm. A Si/Al = 2.0 molar ratio, SiO_2/Na_2O = 0.5 mass ratio and a liquid/solid = 0.4 mass ratio provided high compressive strength to the AAMs owing to the polymerization of BFS. Beyond the scope of this study, these results showed that AAMs based on BFS and calcined alumina are promising materials for the capture of CO_2 at 35 °C with a low partial pressure of CO_2 ($P_{CO_2} = 0.2$). Therefore, future research should focus on further optimizing other properties, such as durability and resistance to sulfate attack, and larger specimens should also be tested, as well as specimens with other geometries (tiles and beams). Finally, an in-depth study on the physicochemical properties and determining the number of basic sites available on the surface of AAMs should be conducted, which is of great importance in determining the AAM-CO_2 affinity (solid–gas).

Author contributions

Tania Ariadna García-Mejía: conceptualization, methodology, investigation, visualization, writing – original draft. Efraín Ovando-Shelley: resources, project administration, supervision, writing – review and editing. Rosa María Ramírez-Zamora: conceptualization, resources, project administration, supervision, writing – review and editing.

Conflicts of interest

The authors declare that they have no known competing financial interests or personal relationships that could have influenced the work reported in this study.

Data availability

The data are available from the corresponding author upon reasonable request.

Supplementary information is available. See DOI: **https://doi.org/10.1039/d5ta04420k**.

Acknowledgements

This journal is © The Royal Society of Chemistry 2025

J. Mater. Chem. A, 2025, **13**, 38080–38093 | **38091**

References

1 Y. Wang, L. Chen, S. Li and Z. Zhang, *Sep. Purif. Technol.*, 2025, **354**, 129114.

2 H. Zhang, J. Cui, Y. Peng, Y. Zhao and Y. Pei, *J. Cleaner Prod.*, 2025, **519**, 146004.

3 C. Di Pietro, W. F. Cossio Guzman, E. Papa, E. Landi, F. Miccio, M. Minelli and V. Medri, *J. Environ. Chem. Eng.*, 2025, **13**, 117098.

4 K. L. Scrivener, V. M. John and E. M. Gartner, *Cem. Concr. Res.*, 2018, **114**, 2–26.

5 Y. Wu, B. Lu, T. Bai, H. Wang, F. Du, Y. Zhang, L. Cai, C. Jiang and W. Wang, *Constr. Build. Mater.*, 2019, **224**, 930–949.

6 T. Wang, DOI:available:%0A **https://www.statista.com/statistics/219343/cementproductionworldwide/#::text=Cementproductionreachedanestimated**, in 2019 in the U.S.

7 R. M. Andrew, *Earth Syst. Sci. Data*, 2018, **10**, 195–217.

8 R. M. Andrew, *Earth Syst. Sci. Data*, 2019, **11**, 1675–1710.

9 E. Benhelal, E. Shamsaei and M. I. Rashid, *J. Environ. Sci.*, 2021, **104**, 84–101.

10 V. Sousa and J. A. Bogas, *J. Cleaner Prod.*, 2021, **306**, 127277.

11 L. E. Menchaca-Ballinas and J. I. Escalante-Garcia, *J. Cleaner Prod.*, 2019, **239**, 117992.

12 J. L. Provis, *Cem. Concr. Res.*, 2018, **114**, 40–48.

13 S. Luhar, T. W. Cheng, D. Nicolaides, I. Luhar, D. Panias and K. Sakkas, *Constr. Build. Mater.*, 2019, **220**, 547–564.

14 Z. Ji and Y. Pei, *J. Environ. Manage.*, 2019, **231**, 256–267.

15 S. A. Rasaki, Z. Bingxue, R. Guarecuco, T. Thomas and Y. Minghui, *J. Cleaner Prod.*, 2019, **213**, 42–58.

16 P. N. Lemougna, K. tuo Wang, Q. Tang, U. C. Melo and X. min Cui, *Ceram. Int.*, 2016, **42**, 15142–15159.

17 J. Zhang, J. Wang, S. Dong, X. Yu and B. Han, *Composites, Part A*, 2019, **125**, 105533.

18 M. Minelli, V. Medri, E. Papa, F. Miccio, E. Landi and F. Doghieri, *Chem. Eng. Sci.*, 2016, **148**, 267–274.

19 E. Papa, V. Medri, S. Amari, J. Manaud, P. Benito, A. Vaccari and E. Landi, *J. Cleaner Prod.*, 2018, **171**, 76–84.

20 E. Papa, V. Medri, C. Paillard, B. Contri, A. Natali Murri, A. Vaccari and E. Landi, *J. Cleaner Prod.*, 2019, **237**, 117738.

21 P. Chindaprasirt and U. Rattanasak, *Int. J. Greenhouse Gas Control*, 2019, **85**, 30–35.

22 H. Chen, Y. J. Zhang, P. Y. He, C. J. Li and L. C. Liu, *Microporous Mesoporous Mater.*, 2020, **305**, 110282.

23 A. L. Freire, C. D. Moura-Nickel, G. Scaratti, A. De Rossi, M. H. Araújo, A. De Noni Júnior, A. E. Rodrigues, E. R. Castellón and R. de Fátima Peralta Muniz Moreira, *J. Cleaner Prod.*, 2020, **273**, 122917.

24 S. S. Hossain and F. Akhtar, *J. CO$_2$ Util.*, 2023, **78**, 102631.

25 B. Dziejarski, J. Serafin, K. Andersson and R. Krzyżyńska, *Mater. Today Sustainability*, 2023, **24**, 100483.

26 J. Wang, L. Huang, R. Yang, Z. Zhang, J. Wu, Y. Gao, Q. Wang, D. O'Hare and Z. Zhong, *Energy Environ. Sci.*, 2014, **7**, 3478–3518.

27 Y. Wang, X. Liu, W. Zhang, Z. Li, Y. Zhang, Y. Li and Y. Ren, *J. Cleaner Prod.*, 2020, **244**, 118852.

28 B. Aouan, S. Alehyen, M. Fadil, M. EL Alouani, A. Khabbazi, A. Atbir and M. Taibi, *Chem. Data Collect.*, 2021, **31**, 100636.

29 H. Zhang, Z. Ji, Y. Zeng and Y. Pei, *Chemosphere*, 2022, **288**, 132495.

30 E. Papa, M. Minelli, M. C. Marchioni, E. Landi, F. Miccio, A. Natali Murri, P. Benito, A. Vaccari and V. Medri, *Appl. Clay Sci.*, 2023, **237**, 106900.

31 S. Candamano, A. Policicchio, G. Conte, R. Abarca, C. Algieri, S. Chakraborty, S. Curcio, V. Calabrò, F. Crea and R. G. Agostino, *J. Cleaner Prod.*, 2022, **330**, 129843.

32 L. Han, X. Wang, B. Wu, S. Zhu, J. Wang and Y. Zhang, *J. Cleaner Prod.*, 2022, **372**, 133591.

33 W. Lu, J. Li, G. Qi, X. Hu, Q. Zhang, M. Wang and M. Zhang, *Environ. Sci. Pollut. Res.*, 2023, **30**, 27303–27314.

34 H. Chen, Y. J. Zhang, P. Y. He, C. J. Li and L. C. Liu, *Microporous Mesoporous Mater.*, 2020, **305**, 110282.

35 M. Minelli, E. Papa, V. Medri, F. Miccio, P. Benito, F. Doghieri and E. Landi, *Chem. Eng. J.*, 2018, **341**, 505–515.

36 F. Farooq, X. Jin, M. Faisal Javed, A. Akbar, M. Izhar Shah, F. Aslam and R. Alyousef, *Constr. Build. Mater.*, 2021, **306**, 124762.

37 L. Li, J. Xie, B. Zhang, Y. Feng and J. Yang, *Constr. Build. Mater.*, 2023, **368**, 130389.

38 J. Mishra, B. Nanda, S. K. Patro and R. S. Krishna, *Constr. Build. Mater.*, 2024, **417**, 135242.

39 Y. K. Cho, S. W. Yoo, S. H. Jung, K. M. Lee and S. J. Kwon, *Constr. Build. Mater.*, 2017, **145**, 253–260.

40 H. Cheng, K. L. Lin, R. Cui, C. L. Hwang, Y. M. Chang and T. W. Cheng, *Constr. Build. Mater.*, 2015, **95**, 710–720.

41 K. Juengsuwattananon, F. Winnefeld, P. Chindaprasirt and K. Pimraksa, *Constr. Build. Mater.*, 2019, **226**, 406–417.

42 A. G. Díaz, S. Bueno, L. P. Villarejo and D. Eliche-Quesada, *Constr. Build. Mater.*, 2024, **413**, 134823.

43 S. Sasui, G. Kim, A. Van Riessen, C. Lim, H. Eu, J. Park and J. Nam, *J. Build. Eng.*, 2024, **98**, 111255.

44 S. D. Wang and K. L. Scrivener, *Cem. Concr. Res.*, 1995, **25**, 561–571.

45 A. Fernández-Jimenez and F. Puertas, *Mater. Construcción*, 1997, **1997**, 31–42.

46 F. Puertas and M. Torres-Carrasco, *Cem. Concr. Res.*, 2014, **57**, 95–104.

47 X. Chen, A. Meawad and L. J. Struble, *J. Am. Ceram. Soc.*, 2014, **97**, 3270–3275.

48 P. Duxson, A. Fernández-Jiménez, J. L. Provis, G. C. Lukey, A. Palomo and J. S. J. Van Deventer, *J. Mater. Sci.*, 2007, **42**, 2917–2933.

49 D. E. Angulo-Ramírez, R. Mejía de Gutiérrez and F. Puertas, *Constr. Build. Mater.*, 2017, **140**, 119–128.

38092 | *J. Mater. Chem. A*, 2025, **13**, 38080–38093

This journal is © The Royal Society of Chemistry 2025

50 J. Zhao, L. Tong, B. Li, T. Chen, C. Wang, G. Yang and Y. Zheng, *J. Cleaner Prod.*, 2021, **307**, 127085.

51 F. Puertas, C. Varga and M. M. Alonso, *Cement Concr. Compos.*, 2014, **53**, 279–288.

52 I. H. Aziz, M. M. A. B. Abdullah, M. A. A. Mohd Salleh, E. A. Azimi, J. Chaiprapa and A. V. Sandu, *Constr. Build. Mater.*, 2020, **250**, 118720.

53 P. Duxson, J. L. Provis, G. C. Lukey, S. W. Mallicoat, W. M. Kriven and J. S. J. Van Deventer, *Colloids Surf., A*, 2005, **269**, 47–58.

54 D. Zhang, T. Zhu, Q. Yang, V. Vandeginste and J. Li, *Constr. Build. Mater.*, 2024, **438**, 137190.

55 A. Alzaza, K. Ohenoja, F. U. Ahmed Shaikh and M. Illikainen, *J. Build. Eng.*, 2022, **57**, 104879.

56 C. Wang, G. Ye, Q. Jin, Z. Zhou, D. Hu and Y. Wei, *Constr. Build. Mater.*, 2025, **459**, 139820.

57 P. Cong and Y. Cheng, *J. Traffic Transp. Eng., Engl. Ed.*, 2021, **8**, 283–314.

58 S. Lowell, J. E. Shields, M. A. Thomas and M. Thommes, *Characterization of Porous Solids and Powders: Surface Area, Pore Size and Density*, Springer Netherlands, Dordrecht, 2004, vol. 16.

59 K. S. W. Sing, *Pure Appl. Chem.*, 1982, **54**, 2201–2218.

60 I. S. Ismail, G. Singh, P. Smith, S. Kim, J. H. Yang, S. Joseph, S. Yusup, M. Singh, V. Bansal, S. N. Talapaneni and A. Vinu, *Carbon*, 2020, **160**, 113–124.

61 P. Sazama, O. Bortnovsky, J. Dědeček, Z. Tvaržková and Z. Sobalík, *Catal. Today*, 2011, **164**, 92–99.

62 R. Cioffi, L. Maffucci and L. Santoro, *Resour., Conserv. Recycl.*, 2003, **40**, 27–38.

63 N. Narayanan and K. Ramamurthy, *Cement Concr. Compos.*, 2000, **22**, 321–329.

64 J. Zhang, Y. He, Y. P. Wang, J. Mao and X. M. Cui, *Mater. Lett.*, 2014, **116**, 167–170.

65 M. Cyr and R. Pouhet, *Cem. Concr. Res.*, 2016, **88**, 227–235.

66 J. Davidovits, *J. Therm. Anal.*, 1991, **37**, 1633–1656.

67 D. M. Degefu, Z. Liao, U. Berardi and G. Labbé, *J. Non-Cryst. Solids*, 2022, **582**, 121432.

68 E. Kamseu, B. Nait-Ali, M. C. Bignozzi, C. Leonelli, S. Rossignol and D. S. Smith, *J. Eur. Ceram. Soc.*, 2012, **32**, 1593–1603.

69 P. Duxson, S. W. Mallicoat, G. C. Lukey, W. M. Kriven and J. S. J. van Deventer, *Colloids Surf., A*, 2007, **292**, 8–20.

70 Z. Peng, Z. Liu, Y. Gao, J. Liu, D. Wang, H. Liu, Y. Zhang and L. Li, *J. Environ. Chem. Eng.*, 2023, **11**, 110837.

71 X. H. Yan, P. Li, H. Yuan, W. Huang, Z. Hu and R. T. Yang, *Sep. Purif. Technol.*, 2025, **354**, 129304.

72 A. Patil, A. Patel and R. Purohit, *Mater. Today: Proc.*, 2017, **4**, 3807–3815.

73 L. G. T. Gouveia, C. B. Agustini, O. W. Perez-Lopez and M. Gutterres, *J. Environ. Chem. Eng.*, 2020, **8**, 103823.

74 A. Maleki, M. Mohammad, Z. Emdadi, N. Asim, M. Azizi and J. Safaei, *Arabian J. Chem.*, 2020, **13**, 3017–3025.

75 Z. Emdadi, N. Asim, M. H. Amin, M. A. Yarmo, A. Maleki, M. Azizi and K. Sopian, *Appl. Sci.*, 2017, **7**, 514.

76 R. M. Novais, L. H. Buruberri, M. P. Seabra and J. A. Labrincha, *J. Hazard. Mater.*, 2016, **318**, 631–640.

77 Y. Wang, L. Liu, C. Ren, J. Ma, B. Shen, P. Zhao and Z. Zhang, *J. Environ. Manage.*, 2024, **349**, 119540.

78 E. Papa, M. Minelli, M. C. Marchioni, E. Landi, F. Miccio, A. Natali Murri, P. Benito, A. Vaccari and V. Medri, *Appl. Clay Sci.*, 2023, **237**, 106900.

79 Q. H. Nguyen, S. Lorente, A. Duhart-Barone and H. Lamotte, *Constr. Build. Mater.*, 2018, **191**, 853–865.

80 Y. Zhang, W. Su, Y. Sun, J. Liu, X. Liu and X. Wang, *J. Chem. Eng. Data*, 2015, **60**, 2951–2957.

81 M. Torres-Carrasco and F. Puertas, *J. Cleaner Prod.*, 2015, **90**, 397–408.

82 J. Davidovits, *Geopolymer Chemistry and Applications*, Geopolymer Institute, Saint-Quentin France, 5th edn, 2008.

83 M. Zahid, N. Shafiq and A. Jalal, *Constr. Build. Mater.*, 2018, **181**, 227–237.

84 A. Aboulayt, M. Riahi, M. Ouazzani Touhami, H. Hannache, M. Gomina and R. Moussa, *Adv. Powder Technol.*, 2017, **28**, 2393–2401.

85 S. K. Nath and S. Kumar, *Constr. Build. Mater.*, 2020, **233**, 117294.

86 A. Bouaziz, R. Hamzaoui, S. Guessasma, R. Lakhal, D. Achoura and N. Leklou, *Powder Technol.*, 2017, **308**, 37–46.

87 J. Peyne, J. Gautron, J. Doudeau, E. Joussein and S. Rossignol, *Constr. Build. Mater.*, 2017, **152**, 794–803.

88 B. Walkley, X. Ke, O. H. Hussein, S. A. Bernal and J. L. Provis, *J. Hazard. Mater.*, 2020, **382**, 121015.

89 J. Y. Lai, L. H. Ngu and S. S. Hashim, *Greenhouse Gases: Sci. Technol.*, 2021, **11**, 1076–1117.

90 O. Cheung, Z. Bacsik, Q. Liu, A. Mace and N. Hedin, *Appl. Energy*, 2013, **112**, 1326–1336.

91 M. M. Zagho, M. K. Hassan, M. Khraisheh, M. A. A. Al-Maadeed and S. Nazarenko, *Chem. Eng. J. Adv.*, 2021, **6**, 100091.

92 Q. Zhang, J. Yu and A. Corma, *Adv. Mater.*, 2020, **32**, 1–31.

93 Y. Yu, J. Mai, L. Wang, X. Li, Z. Jiang and F. Wang, *Sci. Rep.*, 2014, **4**, 1–8.

94 M. Kong, L. Song, H. Liao, S. Zhang, Y. Wang, X. Deng and W. Feng, *Fuel*, 2024, **371**, 132103.

95 D. Chakraborty, A. Yurdusen, G. Mouchaham, F. Nouar and C. Serre, *Adv. Funct. Mater.*, 2024, **34**, 1–23.

96 J. Shaheen, Y. H. Fseha and B. Sizirici, *Heliyon*, 2022, **8**, e12388.

This journal is © The Royal Society of Chemistry 2025

J. Mater. Chem. A, 2025, **13**, 38080–38093 | **38093**